Path and variability of the Agulhas Return Current

Olaf Boebel[a,b,c,*], Tom Rossby[a], Johann Lutjeharms[b], Walter Zenk[d],
Charlie Barron[e]

[a] *Graduate School of Oceanography, University of Rhode Island, Narragansett, 02882 RI, USA*
[b] *Department of Oceanography, University of Cape Town, 7701 Rondebosch, South Africa*
[c] *Alfred Wegener Institute for Polar- and Marine Research, PO 120161, 27515 Bremerhaven, Germany*
[d] *Institut für Meereskunde an der Christian-Albrechts-Universität Kiel, Düsternbrooker Weg 20, 24105 Kiel, Germany*
[e] *Naval Research Laboratory, Stennis Space Center, 39529 MS, USA*

Abstract

The combined analysis of hydrographic, kinematic, and dynamic data collected during the 1997–1999 *KAPEX* (*CAP*e of Good Hope *EX*periments) reveals a quasi-stationary meandering pattern of the Agulhas Retroflection Current east and upstream of the Southwest-Indian Ridge. The current meanders between 38°S and 40°S in a spatially and temporally continuous fashion and has a core width of approximately 70 km with an associated transport of $44 \pm 5 \times 10^6$ m^3 s^{-1} in the upper 1000 m. Peak surface velocities decrease from 2.1 m s^{-1} near the Agulhas Retroflection to 1.1 m s^{-1} around 32°E. Meander troughs (northward extremes) are found predominantly near 26.8°E, 32.6°E and 38.9°E, while crests (southward extremes) are located with high probability near 29.7°E, 35.5°E and 42.9°E, resulting in a typical wavelength of 500 km. Cold eddies are shed along the northern boundary of the current from meander troughs into the recirculation regime between the Agulhas Current proper and the Agulhas Return Current. Strongest cyclonic eddies are preferably shed in austral autumn. The cyclonic eddies so formed propagate westward at an average phase-speed of 5.4 cm s^{-1}, with, however, a variability of at least the same magnitude. Subsequently, the cyclones are absorbed by the next meander trough located upstream and to the west of the shedding trough.
© 2002 Elsevier Science Ltd. All rights reserved.

1. Introduction

Participants of trans-oceanic sailing races on their way to Australia are greatly interested in the location of currents south of Africa. Apart from the Antarctic Circumpolar Current, the most beneficial current to their goal of being the first to reach Australia is the Agulhas Return Current (ARC, Fig. 1). Located nominally along the 39°S parallel, this current exhibits eastward surface velocities of up to 4 knots (≈ 2 m s^{-1}). The Agulhas Return Current emerges from the Agulhas Retroflection (Bang, 1970), i.e. the oceanic region south of the tip of Africa (Fig. 1, label ④). There the southwestward setting Agulhas Current (Fig. 1, ①), which is the western boundary current of the South Indian Ocean, retroflects, feeding the

---

*Corresponding author. Alfred Wegener Institute for Polar- and Marine Research, PO 120161, 27515 Bremerhaven, Germany. Tel.: +49-471-4831-1879; fax: +49-471-4831-1797.

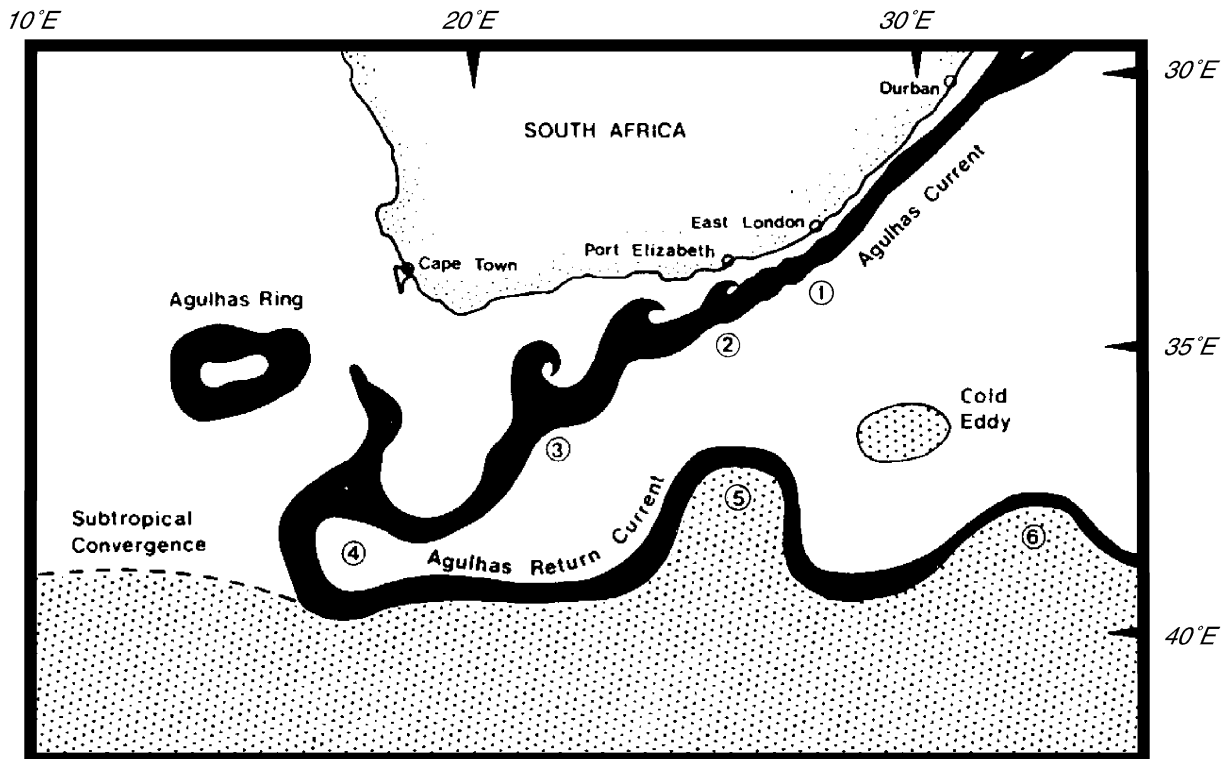*E-mail address:* oboebel@awi-bremerhaven.de (O. Boebel).

Fig. 1. Features of the large-scale circulation of the Agulhas Current system (modified from Lutjeharms and van Ballegooyen (1984)). ① Onset of small meanders in the current; ② divergence of current axis from coast; ③ downstream meanders; ④ Agulhas Current Retroflection; the first (⑤) and a downstream (⑥) meander of the Agulhas Return Current, located over the Agulhas Plateau and farther west, respectively.

ARC and occasionally folding back onto itself, shedding large eddies, i.e. Agulhas Rings (Lutjeharms, 1996).

It is hence not surprising that the structure of the ARC resembles that of the Agulhas Current proper. In particular, the ARC is associated with a temperature front that alternatively has been named Agulhas Front (AF) or Agulhas Convergence (Lutjeharms and Valentine, 1984). We will use the term AF with regard to (historic) hydrographic descriptions of the front, while ARC is applied in the following towards the front's kinematic expression. Various proxy criteria have been developed for the AF (Lutjeharms and Valentine, 1984; Read and Pollard, 1993; Sparrow et al., 1996), and a strong case has been made by Belkin and Gordon (1996) that the depth change of the $10°C$ isotherm ($Temp_{10}$) from shallower than 300 m on the southern side to deeper than

800 m on the northern side provides a stable criterion for the AF between $20°E$ and $40°E$. It must be noted that the $Temp_{10}$ experiences overall shoaling downstream; however, the definition given above is sufficiently accurate for the region discussed here ($15°E$–$45°E$).

A substantial body of research has focused on the location and associated transport of the AF. Most of these studies (Stramma, 1992; Read and Pollard, 1993; Belkin and Gordon, 1996) have used collections of individual hydrographic sections. Based on the *RRS Discovery* cruise no. 164, Read and Pollard (1993) have reported a transport of 84 Sverdrup (1 Sv $= 10^6$ m^3 s^{-1}) for the ARC at $40°S$, $40°E$. Using a vast collection of hydrographic stations, Belkin and Gordon (1996) trace the AF from $15°E$ to $75°E$, while pointing out the existence of two quasi-stationary meanders in the Agulhas Basin. Sparrow et al. (1996) attempt

to identify the AF in gridded hydrographic data (from the Hydrographic Atlas of the Southern Ocean, HASO, (Olbers et al., 1992) and in the FRAM model output (Webb et al., 1991). Sparrow et al. (1996) emphasize in particular that the Agulhas Return Current has its strongest kinematic expression contiguous to the northern edge of the AF. At 30°E, their analysis of HASO-data suggests a merging of the AF with the Subtropical Convergence (sometimes also named Subtropical Front), with velocities of up to 23 cm s^{-1} in an approximately 600 km wide current band, resulting in an associated transport of 95 Sv.

However, as this later study illustrates, these pathway descriptions and transport estimates are subject to considerable uncertainties that arise from the wide station spacing (typically 60 nautical miles) of hydrographic sections (see Read and Pollard (1993) for a detailed discussion), generating a smoothed image of the AF. In many cases, the AF and the adjacent (Southern) Subtropical Convergence have apparently merged. While this might indeed be true in some cases, it also might be an artifact of insufficient resolution of the frontal region. Lutjeharms and Valentine (1984) consequently used additional high-resolution or continuous temperature sections to obtain a sharper image of the front. Their analysis suggests a narrow, intense AF of 96 ± 60 km width, which, they note, is the narrowest of all frontal expressions south of Africa.

The space–time composite of AF observations (Belkin and Gordon, 1996) reveals a remarkably stable position of two meander troughs (T_1 and T_2, see Figs. 2 and 3a) with a crest (C_1) in between.[1] The location of T_1 coincides with the location of the Agulhas Plateau (Fig. 3b), a major

bathymetric obstacle of 400 km meridional extent, lying across the path of the ARC. The Agulhas Plateau rises from an ocean floor of 5000 m to depths between 2500 and 3000 m for its greater part, with isolated peaks reaching shallower than 500 m. However, whether this first meander of the AF is exclusively generated and trapped by topographic steering is open to question. Modeling efforts without a detailed bathymetry (Pichevin et al., 1999) also produce a similar first trough east of the Retroflection, a fact that at least hints towards an additional dynamical factor.

A common problem of the hydrographic studies mentioned above is that individual observations of the fronts are uncorrelated in time, which obviously prohibits any findings regarding the temporal evolution of the (meandering) AF. Thus it is highly desirable to obtain continuous data for this region, in order to construct a spatially coherent and temporally resolved description.

This study has three objectives: (a) to estimate the ARC transport within the upper ocean, (b) to determine its mean pathway, and (c) to expose the current's temporal evolution. After a short description of our data (section Data), the first topic is addressed by calculating the ARC width and average along-stream velocities from four vessel-mounted Acoustic Doppler Current Profiler (ADCP) sections (Near-surface velocities and temperature structure). Subsequently, using a single high-resolution XBT (expendable bathy thermograph) section across the ARC, a generic temperature section is developed (the deep velocity structure). This generic temperature section is then used to determine the lateral position of direct subsurface velocity measurements from subsurface RAFOS (Ranging and Fixing of Sound) float trajectories (Rossby et al., 1986; Schultz Tokos et al., 1994). The resulting velocity field is combined with the ADCP data into a generic velocity section across the ARC, from which transport estimates are made (section Transport). Subsequently, addressing the second topic, the mean pathway of the ARC is established from 3 years of absolute sea-surface steric height anomaly estimates based on altimeter and climatological data. Lastly, the temporal evolution of the current is estimated from this data.

---

[1] Please note our definition of crests and troughs might be reverse to that of others working in the southern hemisphere (e.g. Weeks et al., 1998). While our study considers the South Pole as "up", to maintain a consistent dynamical description with northern hemisphere studies, Weeks et al. use the conventional orientation of maps (north up) as basis for their definition of troughs and crests. Our admittedly disputable convention is based on the concept of the subtropical gyre of which western boundary currents and their extensions are part. To define crests as radially outward extension appears natural for the circular pathways within this gyre.
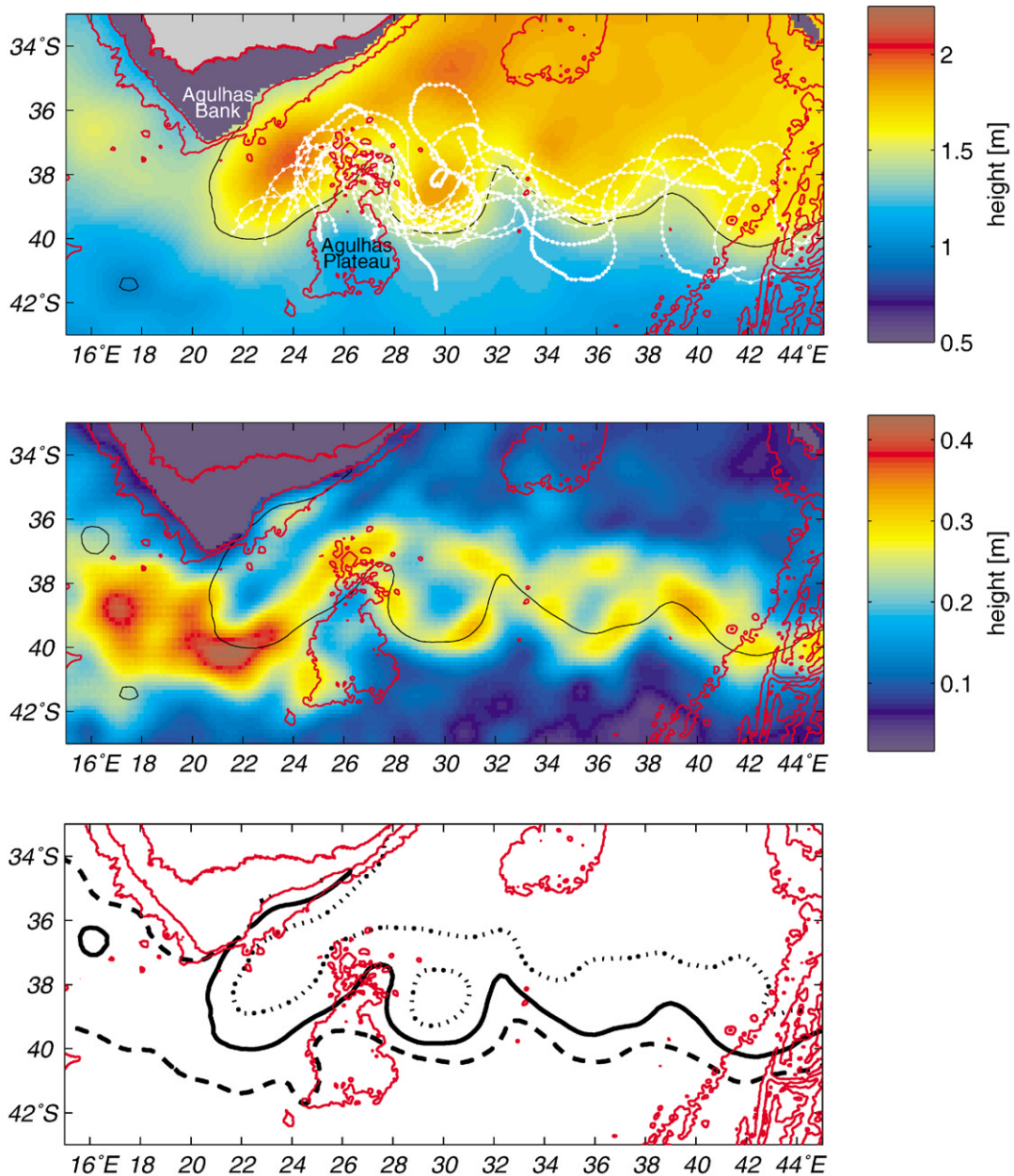
Fig. 2. Top: 3-year (1997–1999) average of MODAS-2D absolute sea-surface steric height anomalies. The 1.5 m SSH isoline is indicated by a thin black line. Selected RAFOS float trajectory segments (white lines with dots) in the ARC region are superposed. Isobaths at 0, 1000 and 3000 m are given in red, and the area above sea level is shaded gray (top panel only), areas shallower than 1000 m are dark blue. All trajectory segments start west of the Agulhas Plateau. Middle: Standard deviation of 3 years of daily sea-surface steric height anomalies. The location of the 1.5 m SSH isoline from the top panel is indicated. Note the difference in color scale with respect to the top panel. Bottom: Positions of the 1.5 m SSH isolines for the mean SSH field (solid line), as well as for the mean ±1 standard deviation (dashed and dotted lines, respectively).
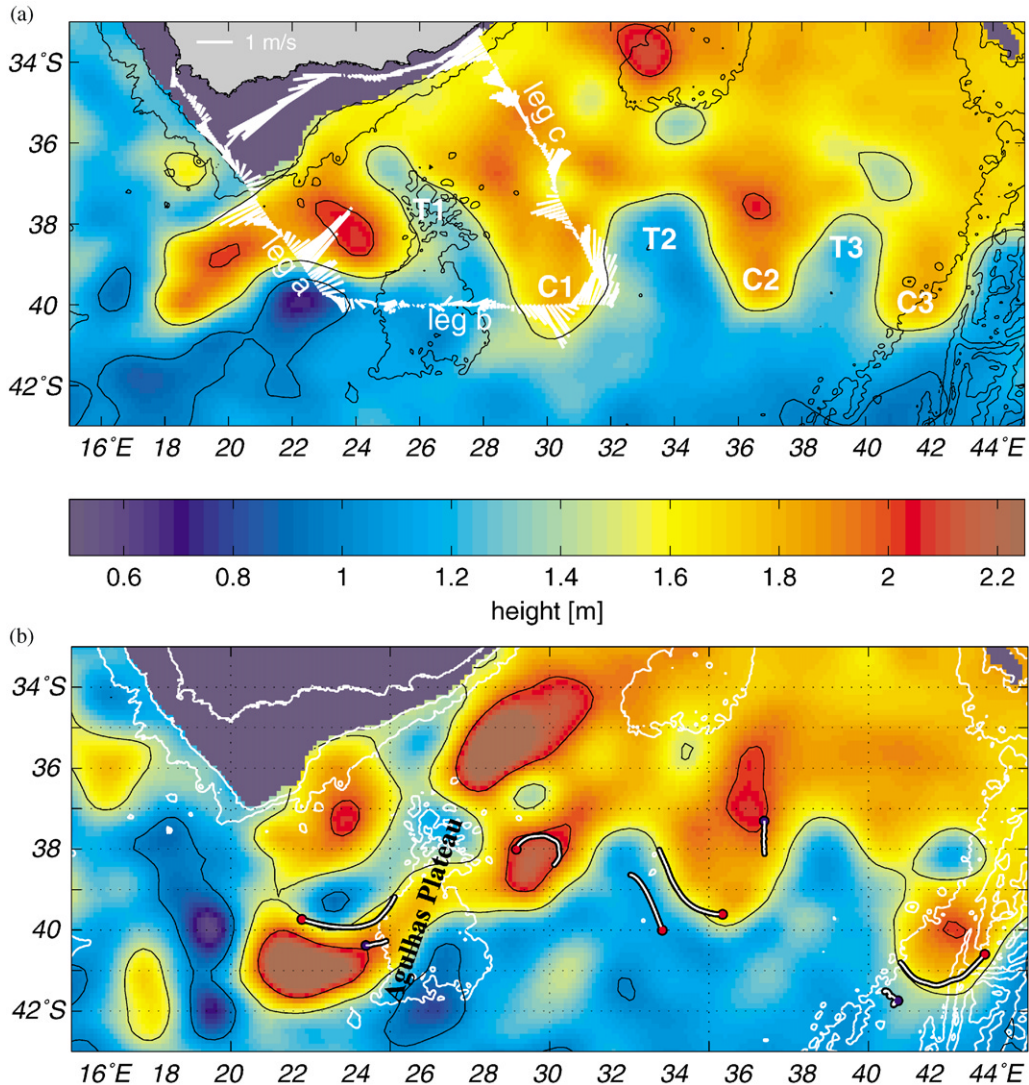
Fig. 3. (a) ADCP velocity data (21–25 m bin) from R/V *Seward Johnson* cruise 97/04 superposed on the (synoptic) MODAS-2D SSH field for 23 August 1997. (b) Seven day float trajectory segments centered at 7 March 1999, the nominal date of the MODAS-2D SSH composite field depicted. Floats are represented by comets (heads first), with red and blue heads representing shallow and deep isopycnal floats.

2. Data

2.1. Lagrangian data

Subsurface velocity data between 200 and 1350 m depth were collected in the ocean sur-rounding South Africa using neutrally buoyant RAFOS floats (Rossby et al., 1986) deployed under the auspices of the KAPEX program (Boebel et al., 1998). Detailed descriptions of float deployment, data acquisition and tracking procedures are given in Boebel et al. (2000). Subsurface positions were obtained at either 12- or 24-h intervals (dots in Fig. 2, top panel), and associated meridional and zonal velocities were estimated from the tangent along splined latitudes

and longitudes, respectively. The data set presented here comprises those floats that became entrained in the meandering ARC.

Interestingly, 8 of the 13 floats trapped by the ARC had been launched in the Atlantic along the southern boundary of the Cape Basin, i.e. to the northwest of the Agulhas Retroflection. (None of the floats was launched deliberately into the ARC.) The isobaric character of these 8 floats prohibits a direct interpretation of these trajectories as *proof* of continuous pathways from the Atlantic to the Indian Ocean. Nevertheless, the existence of such float trajectories necessitates a sequence of flow regimes directed this way, *hinting* towards an Atlantic to Indian Ocean transfer of intermediate water.

2.2. Altimetry

TOPEX/Poseidon and ERS sea-surface height data were processed at the Stennis Space Center's Naval Research Laboratory as part of the Modular Ocean Data Assimilation System (MODAS). The latter is designed to generate synoptic, mesoscale-resolving 3-D hydrographic (T and S) fields from a combination of ocean climatology and quasi-instantaneous satellite (SSH and SST) measurements (Jacobs et al., 2001; Fox et al., 2002). Only the 2-D absolute sea-surface steric height anomalies, which are referenced here as MODAS-2D SSH or simply SSH, are used in this study. The validity of the daily SSH snapshots is evaluated in an accompanying publication (Boebel and Barron, 2003) by comparison with in situ velocity data from RAFOS floats and shipborne ADCP, which concludes that MODAS-2D SSH adequately represents the mesoscale features within the region of the ARC.

2.3. Shipboard data sets

During the R/V *Seward Johnson* cruise 97/04, hull mounted-ADCP and XBT sections were taken during the outbound leg (Fig. 3a, leg a), the zonal leg (Fig. 3a, leg b), and the shore bound leg (Fig. 3a, leg c). Fig. 3a shows the superposition of the 21–25 m bin ADCP data onto the MODAS-2D SSH field of 23 August 1997. Although the

cruise ends 10 days past the nominal date of this SSH image, the graph nevertheless clearly indicates a good agreement between the ADCP data and the MODAS-2D SSH field, and that the ARC was crossed on four occasions. These will be discussed in detail in the following section.

3. The baroclinic structure of the Agulhas Return Current

3.1. Near surface velocities and temperature structure

During the southern part of leg a (Fig. 3a), the first crossing of the ARC occurred near 39°S 22°E, with the current setting in a northeastward direction (43°T). The ADCP section (Fig. 4a) indicates a surface intensified velocity signal reaching 2.1 m s^{-1}. Velocities decrease with depth, but still exceed 1.3 m s^{-1} in the deepest (325–375 m) bin at the current's core. Projecting the ship's transect (145°T) onto a plane normal to the current's direction, the width of the current is determined to be 48 ± 14 km (Table 1). The current width, as given here and in the calculations below, is the median of distances between isotachs of $\frac{1}{2}$ of each layer's respective maximum velocity. The indicated error of the estimated width is based on the distance between subsequent ADCP data points, 9.6 km, assuming that errors in determining the northern and southern edge add independently. Additional possible errors of the width estimate caused by the projection are negligible (1 km), with the projection angle α varying with depth by only a few degrees ($9° < \alpha < 15°$), where α describes the angle between the ship's course and the plane perpendicular to the maximum ADCP velocity vector at each depth.

The second crossing of the current occurred near 30°E of leg b along the 40°S parallel (Fig. 3a; ship's course 90°T). The current flowed southeastward (144°T) into the first crest leeward of the Agulhas Plateau (Fig. 3a; C$_1$). The ADCP data (Fig. 4b) again indicate a surface intensified flow field, with speeds in excess of 1.3 m s^{-1}. The projected width is 73 ± 18 km, including the uncertainty based on the observed range of
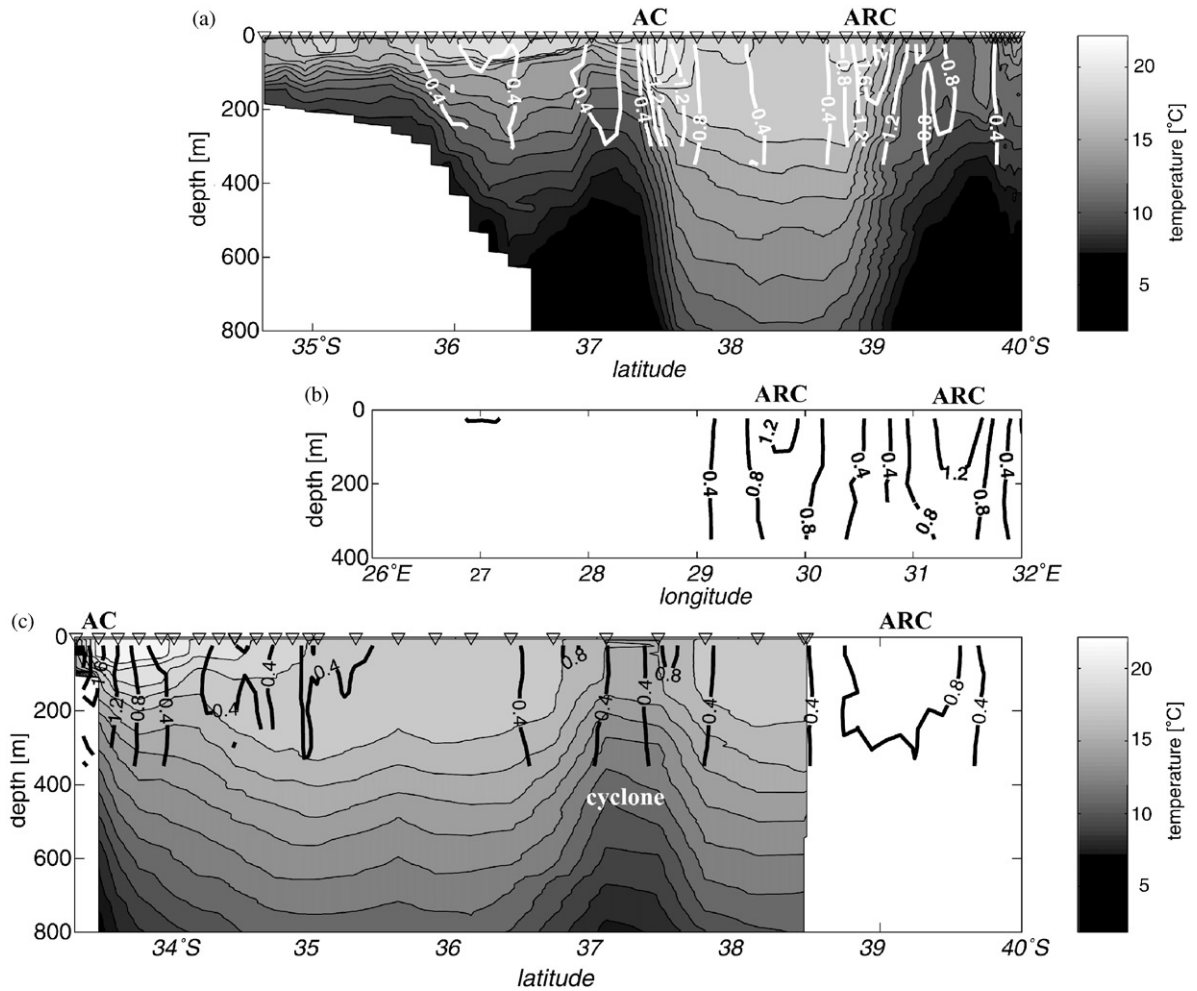
Fig. 4. ADCP sections of legs a–c (top to bottom), combined with XBT sections for leg a and c. ADCP velocities are assigned to the center depth for each bin, e.g. to 350 m for the 325–375 m bin. The x-axes are scaled to be approximately equidistant for the three subplots. Positions of the Agulhas Current (AC), the Agulhas Return Current (ARC) and of a cyclonic eddy are indicated.

Table 1
Estimates of the Agulhas Return Current width with errors from ADCP sections

	Leg a	Leg b, 1st crossing	Leg b, 2nd crossing	Leg c
Width and total error estimate (km)	48 ± 14	73 ± 18	78 ± 18	48 ± 18
Projection uncertainty (km)	1	6	1	17
Maximum speed near 25 m (m s^{-1})	2.1	1.3	1.5	1.1
Maximum speed at 350 m (m s^{-1})	1.3	1.0	0.9	0.8

the projection angles ($25° < \alpha < 41°$). At the maximum ADCP depth bin (325–375 m) maximum speeds are greater 1.0 m s^{-1}.

Slightly farther east, near 31.5°E, the cruise track crosses the north-northeastward setting current (19°T) returning out of crest C_1. Velocity

values > 1.5 m s^{-1} are observed near the surface, and the estimated width has increased to 78 ± 18 km. Weak baroclinic current shear results in a small range of projection angles $16° < \alpha < 21°$, which again give rise to a negligible additional error of 1 km. The current core speed is above 0.9 m s^{-1} at the lower limit of the ADCP measurements (nominally 350 m).

The fourth crossing of the current occurred during the subsequent northbound leg c (ship's course 335°T) near 39°S (Fig. 4c). Directly adjacent to the previous crossing, in the transition region between crest C_1 and trough T_2 (Fig. 3a), the current swung towards the north (6°T), and crossed leg c obliquely at an angle of about 20°. The maximum speed was > 1.1 m s^{-1}, significantly less than the value of 1.5 m s^{-1} observed upstream. A mean width of 48 ± 18 km is obtained, including the large uncertainty (17 km) introduced by the range of large projection angles ($62° < \alpha < 78°$). The significant scatter of these angles reflects the divergent nature that the current had assumed here. At 350 m depth, the maximum speed is reduced slightly to 0.8 m s^{-1}, showing little deviation from the observations directly upstream. While this and the previous crossing of the ARC are in close spatial proximity, they are separated in time by approximately 1 day, due to mooring operations between leg b and leg c.

Averaging these four estimates of the current's width results in our best guess value of 62 ± 9 km. To examine the variability between the sections further, the four ARC crossings are each centered at the position of its maximum velocity vector and projected onto a plane perpendicular to their respective main current direction (Fig. 5). Superposition of the resulting velocity sections clearly indicates a strong variability in between sections, even stronger than the baroclinic structure observed within the upper 350 m of each section. Only the two sections representing the in- and outflow of crest C_1 exhibit a similar structure (Fig. 5, green and blue curves). The asymmetry of these two profiles (the anticyclonic side extends to about 50 km while the cyclonic side is truncated at 35 km distance) is probably related to them representing a region of strong curvature flow,

i.e. crest C_1, while the other two sections from regions of straight flow are of lesser asymmetry.

Our directly measured surface peak velocities lie between 2.1 and 1.1 m s^{-1}, exceeding the values derived by previous geostrophic estimates significantly. Lutjeharms and Ansorge (2001) for example report ARC (surface) geostrophic speeds relative to 1500 m of 0.75 m s^{-1} near the Agulhas Retroflection. The discrepancies between geostrophic and directly observed peak velocities can be due to the large station spacing of the hydrographic sections (typically order of 100 km), which fail to resolve the high-velocity core. Averaging our direct surface velocity values over the four crossings and the current's full core width (i.e. where the flow exceeds $\frac{1}{2}$ of its maximum speed) results in an average core speed of 1.15 m s^{-1}.

Concurrent XBT sections exist for the outbound leg (a) and for part of the inbound leg (c). Unfortunately, the ARC had already been traversed when the second XBT section commenced after some technical difficulties with the XBT probes. Temperature and velocity data during leg a (Fig. 4a) are consistent in their respective description of the oceanic features, indicating a strong geostrophic component of the ARC's velocity signal. Fig. 4a further shows the Agulhas Current proper near 37.5°S as a steep drop of the isotherms, underlying a surface temperature maximum ($> 20°C$), which is coincident with a high-speed core (> 1.2 m s^{-1}). Interestingly, this maximum speed is significantly less than the 2.1 m s^{-1} observed approximately of 1000 km downstream at the first crossing of the ARC (Fig. 3a). The ARC's kinematic signal is echoed by the steep rise of the isotherms near 39°S. The baroclinic velocity signal of the upper 350 m is directly related to the steeply inclined temperature structure.

During the northbound leg c, a cyclonic cold-core eddy was intercepted just south of 37°S. The cyclonic eddy signal is visible both in the XBT data as a doming of the isotherms by about 300 m, and in the ADCP data in the form of two velocity cores in excess of 0.8 m s^{-1}. At the continental shelf the Agulhas Current proper flows at speeds greater than 2.4 m s^{-1}, with surface temperatures above
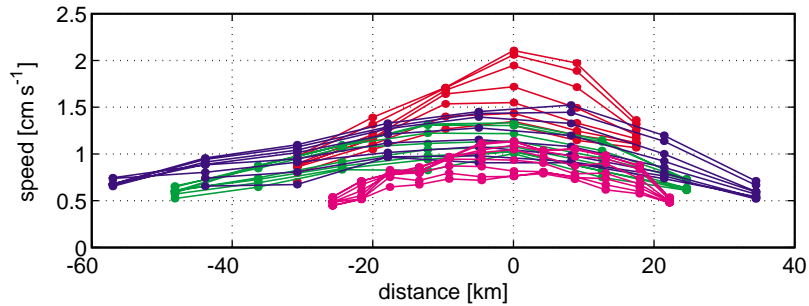
Fig. 5. Projected ADCP sections across the ARC. Each section consists of several profiles representing various depth bins centered at 25 m and successively between 50 and 350 m depth, with 50 m bin width. Crossing are color coded red, green, blue and cyan for the 1st, 2nd, 3rd and 4th crossing.

20°C and a shoaling of the isotherms in excess of 300 m (Fig. 4).

3.2. The deep velocity structure

An average ARC velocity field can be derived directly from the absolute RAFOS float velocity data, provided it is possible to determine a float's lateral position relative to the current's center. In an analogous situation for the Gulf Stream, Hendry (1988) developed a thermal model based on data from five hydrographic cruises. Bower and Rossby (1989) made a similar attempt, assuming that the thermal structure of the current remains unchanged along the downstream axis, the so-called rigid field assumption. They developed a model of the current's thermal structure based on a 3-year mean temperature section (in natural coordinates, i.e. the downstream and cross-stream directions). In contrast to both these studies, we unfortunately have only one natural coordinate-based temperature section available while hydrographic data from alternative cruises did not provide sufficient horizontal resolution. We hence cannot follow the detailed statistical analysis made by Hendry (1988) and Bower and Rossby (1989) but adopt directly the analytical function developed by Hendry, i.e. to model the temperature dependence by tangent hyperbolic functions in both the vertical (p) and horizontal (x) directions. Using Hendry's naming conventions and in close association with his equations (A1) and (A5), the

functions used are

$$T(p, x) = A \tanh[B(C(x) - p)] + D$$

with

$$C(x) = A_x \tanh[B_x(x - C_x)] + D_x$$

with A, B, D and A_x, B_x, C_x, and D_x, being free parameters. Note that our second equation has, in comparison with Hendry's equation A5, the argument of the tangent hyperbolic multiplied by -1 to accommodate for the southern hemisphere situation. The variable x is positive on the cyclonic and negative on the anticyclonic side of the current. Also the parameters A, B and D were chosen to be constant, i.e. not a function of C as in Hendry (1988), due to the sparseness of data. To optimize the fit at those depths where it will be used to find the floats' lateral positions relative to the current's center, we restrict the fitting procedure to depths greater than 500 m (thicker parts of observed isotherms, i.e. white lines, shown in Fig. 6). A fit of the five free parameters to the smoothed temperature profiles resulted in a root mean error of $\Delta T = 0.27°C$ with the following parameter set: $A = 8.29°C$; $B = (707.5 \text{ m})^{-1}$; $D = 8.19°C$; $A_x = 439.3 \text{ m}$; $B_x = (-43.3 \text{ km})^{-1}$; $C_x = 2.72 \text{ km}$; $D_x = 719.7 \text{ m}$. With regard to lateral positioning of the floats, the temperature rms-error translates into a horizontal uncertainty of less than 10 km, which is only a fraction of the current's width as derived from the ADCP data (62 km). The resulting temperature field depicts
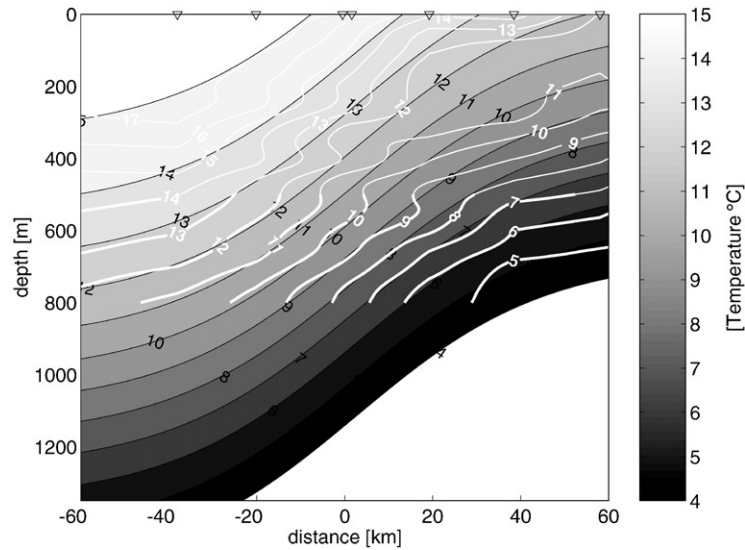
Fig. 6. XBT-based temperature section (white lines) superposed on model temperature field (black contours and shading) fitted to data below 500 m depth (thick part of white lines). The figure enlarges the ARC segment of the temperature section depicted in Fig. 4a.

the 10°C isotherm at 290 m depth at the southern end of the section and at 870 m at its northern limit (at ± 35 km distance from center, respectively). This is in reasonable agreement with the definition of Belkin and Gordon (1996) as given in the introduction (Temp_{10} shallower 300 m at southern and deeper 800 m at northern AF limit).

Using the modeled temperature field, we then mapped the cross-stream position of selected float trajectory segments. Trapping of the floats by the ARC was considered likely when the trajectory showed a meandering path and was located within the vicinity of the mean ARC location as derived from MODAS-2D SSH. This pre-selection (Table 2) resulted in a set of 1985 data points. Fig. 2 shows the similarity of the meanders observed in these subjectively selected float trajectory segments. The corresponding pressure and temperature data from these float trajectory segments were then mapped onto the model temperature field (Fig. 7). Floats were considered to be within the current if the float speed was greater than 10 cm s^{-1} and if the distance from the center was $\leqslant 70$ km. This value (applied towards both sides of the current core) corresponds approximately to twice the current width as

estimated from the ADCP and XBT sections. This condition reduced the number of accepted data points to 1259, while it did not change the meandering trajectory pattern significantly. Only the smaller scale recirculation loops visible in Fig. 2, top panel, i.e. at 38°S 30°E were eliminated.

To estimate the ARC's baroclinic velocity structure, float and ADCP velocities were then combined into a single generic velocity section. Binning and averaging the float data in 100 m (vertical) $\times 10$ km (lateral) boxes on a 50 m $\times$ 5 km grid, yielded a statistical estimate of the deep velocity field. In parallel, the four projected ADCP sections depicted in Fig. 5 were adjusted to a uniform width of 70 km. Then they were bin-averaged within 10 km boxes on a 5 km horizontal grid while maintaining the original vertical sampling bins. Normalizing the sections to a standard width avoided the introduction of an artificial horizontal structure by the averaging process as a result of sections truncating at different distances. By horizontal alignment of the bin averaged maximum ADCP velocity with the box of maximum (averaged) float velocities, a series of vertical velocity profiles was obtained at 5 km intervals. In order to interpolate between the ADCP and

Table 2

Selected float trajectory segments. T_N and C_N stand for the Nth trough and crest as indicated in Fig. 3a. Individual trajectories are presented in Boebel et al. (2000)

| Float #	Segment start (d m y)	Segment end (d m y)	Float type	Comment
183	25 12 1997	1 03 1998	Isobaric	T_1—expelled to south while flowing into C_1
186	1 03 1998	1 04 1998	Isobaric	T_1 (partially tracked)—expelled to south while flowing into C_1
195	1 07 1997	5 08 1997	Isobaric	T_1–C_1—expelled to north while flowing into T_2
195	15 02 1998	5 04 1998	Isobaric	T_1–C_1 (incl. local recirc.)—expelled north while flowing into T_2
196	20 09 1997	1 11 1997	Isobaric	T_1–C_1—expelled north while flowing into T_2
203	10 07 1997	1 02 1998	Isobaric	T_1–C_1–T_2–C_2–T_3—expelled north at C3
217	1 11 1997	15 04 1998	Isobaric	T_1–C_1–T_2–C_2–T_3—expelled south at C3
221	15 06 1998	15 09 1998	Isobaric	T_1–C_2–T_2
222	25 05 1998	15 06 1998	Isobaric	T_1—expelled into southern local recirc. (float sinks due to leak)
499	15 11 1998	1 03 1999	Isopycnal (27.2)	T_1–C_1–T_2–C_2–T_3—surface while probably still in current
503	01 11 1998	15 11 1998	Isopycnal (26.8)	Early retroflection–C_1–local recirculation
503	20 12 1998	15 03 1999	Isopycnal (26.8)	C_1–T_2–C_2–T_3–C_3—surfaces while still in current
512	10 03 1999	1 06 1999	Isopycnal (26.8)	T_1–fast recirculation–C_1–T_2–C_2
513	10 02 1999	1 05 1999	Isopycnal (26.8)	T_1–local recirculation–T_1–C_1–T_2–C_2
519	1 11 1998	1 02 1999	Isopycnal (27.2)	T_1–C_1–T_2–C_2–T_3—expelled to south while flowing into C_3
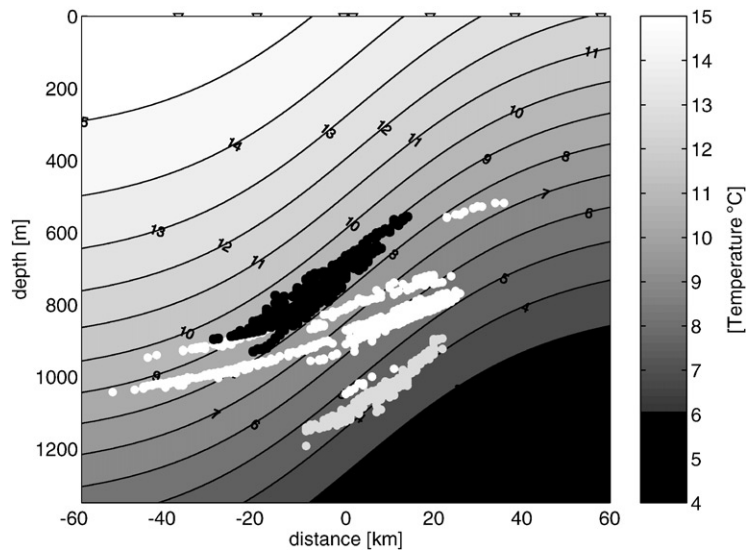
Fig. 7. Float locations within the ARC, mapped onto model temperature filed. The two groups of floats ballasted for $\sigma_\theta = 26.8$ and 27.2, respectively, can clearly be distinguished (black and gray dots). These floats follow closely the isothermal structure (which is assumed to be close to the isopycnal structure). Isobaric floats (white dots) follow the isopycnals to a lesser extent.

RAFOS data, these were fitted independently with a smoothed spline function (Fig. 8a, smoothing coefficient 2×10^{-6}), with a resulting rms error of 3.0 cm s^{-1}.

3.3. Transport

Integration of these mapped velocities (Fig. 8b) for the region of ± 35 km from the velocity

maximum results in a transport of 44 Sv for the upper 1000 m. What is the significance of this estimate? Firstly, a formal error due to the fitting process can be estimated from the rms velocity error given above by applying it towards the full width (70 km) and depth range (1000 m), which results in a error of ± 2 Sv. Secondly, systematic false positioning of the floats by the mapping process could introduce an independent, systematic error. Testing the impact of varying model temperature fields resulted in transports deviating by not more than ± 2 Sv from the result presented above.

Greater uncertainty is introduced through the choice of the current's width. Varying the assumed current width by ± 9 km (the standard deviation of the observed ADCP widths) yields a transport variation of ± 4 Sv. In combination with the ± 2 Sv estimated for each fitting and mapping errors, the total error is estimated at ± 5 Sv.

This error is of the same magnitude as the observed natural current variability. The transport within the upper 375 m for example results in 25, 21, 24, and 17 Sv for the four ADCP sections, respectively (when estimated directly), obtaining 4 Sv standard deviation from their mean. For the lower 600 m between 500 and 1000 m, binned float velocities result in a transport of 7 Sv, with 2 Sv inherent variability. However, the natural variability is already included in our previous error estimate since the data used therein encompass different locations and times. Thus, our transport estimate for the ARC above 1000 m and within the current core, i.e. between isotachs of $\frac{1}{2}$ the peak layer velocity, is 44 ± 5 Sv.

How representative is our spatially limited estimate for the entire current? Fig. 8b shows that considerable flow exists even at distances greater ± 40 km from the center. The assumption of a simple current profile that decreases linearly width distance gives a ballpark estimate of $\frac{1}{4}$ the total transport, i.e. about 11 Sv, to be hidden in the current's lobes. Our result of 44 ± 5 Sv hence possibly underestimates the upper 1000 m transport by up to 11 Sv.

Directly measured velocities within the 1000–1150 m depth range still average at 25 ± 4 cm s^{-1}. Assuming this value to decay linearly to 0 cm s^{-1}

between 1000 and 1500 m depth results in 4 Sv additional transport below our area of directly observed velocities, providing a total transport of 48 Sv above 1500 m. This estimate is particularly interesting because it indicates consistency between our and the independent results of Lutjeharms and Ansorge (2001) from hydrographic sections, stating a volume transport of 47 Sv relative to 1500 m.

Read and Pollard (1993) estimated a significantly enhanced ARC transport of 84 Sv top to bottom. To match our results and those of Lutjeharms and Ansorge (2001) to those of Read and Pollard's, a residual current of order 10 cm s^{-1} would be required for the water column below 1500 m. This appears to be high, but not impossible. However, the possibility to narrow down the ARC transport to a single universal value with small error appears unlikely in view of the ARC's significant variability, as reported by Lutjeharms and Ansorge (2001), directly illustrated by our four ADCP sections, and furthermore shown by the waxing and waning of the MODAS-2D SSH field in the ARC region. The later are discussed in detail in the following section.

4. The Agulhas Return Current's path

The following discussion is founded on the analysis of gridded MODAS-2D SSH fields. It is not immediately evident that these fields should give a proper representation of the ARC, or the Agulhas region in general. Difficulties in obtaining absolute SSH fields from altimetric measurements in the presence of strong quasi-permanent features such as the ARC are well known. However, in the accompanying paper by Boebel and Barron (2003) in this issue, it is shown explicitly for the ARC region through statistical comparison between MODAS-2D, ADCP and RAFOS float data that MODAS-2D gives indeed an appropriate representation of the surface velocity field in general and the evolution/propagation of mesoscale features in particular. Especially the direction of the flow field, which can be seen as a proxy of the overall flow pattern, is highly correlated between
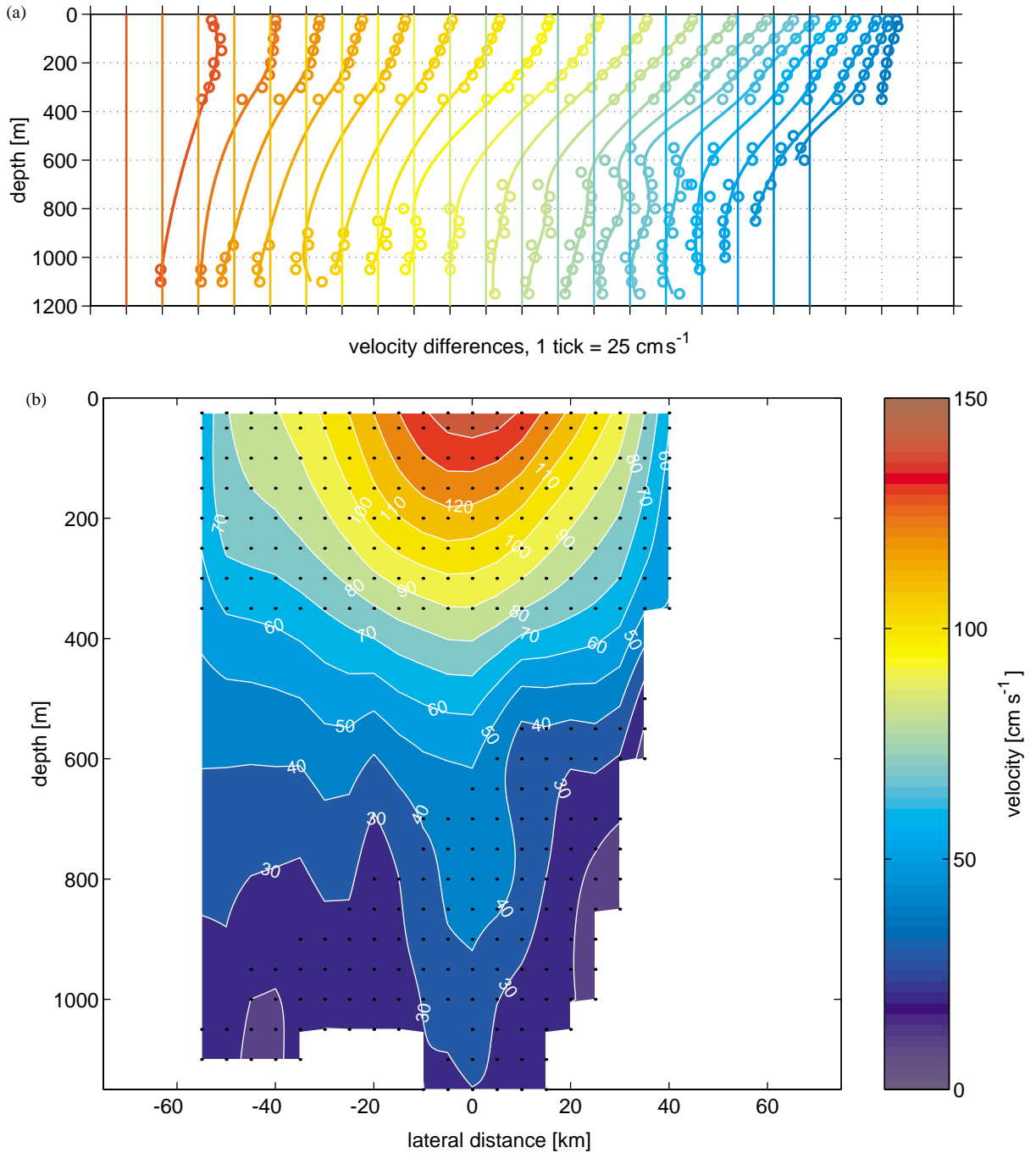
Fig. 8. (a) Velocity data (circles) and interpolated profiles (curves) from boxed ADCP and RAFOS float data. (b) Lateral section of ARC velocities from interpolated velocity profiles. The color bar indicates downstream velocity. The locations of boxes containing valid data are indicated by small black dots.

the three data types. The agreement between these different data sets (views) of the same dynamical system is a strong justification of MODAS-2D for the following analyses. An example is given in Fig. 3b (bottom) where 7-day-long float trajectory segments are superposed on the quasi-synoptic MODAS-2DSSH field of 7 March 1999. For further details please refer to Boebel and Barron (2003).

4.1. Geographically trapped meander positions

The mean path of the ARC, as observed by MODAS-2D SSH, is depicted in Fig. 2, top panel (color and thin black line). Our study shows the meandering ARC as flowing eastward between 38° and 40°S latitude, with a tendency towards higher latitudes farther east. The meridional variability (one standard deviation) covers the 36°–40°S range near the Agulhas Plateau, whereas a 37°–41°S range is observed farther west (40°E). These findings fall in line with results from previous studies, as subsumed by Lutjeharms and Ansorge (2001), who position the average latitude of the ARC at 39.5°S for the region south of Africa and at higher latitudes farther east. Around this mean axis, the ARC appears to undulate in a remarkable stable pattern. Three crests and troughs are evident (Table 3) in the 3-year MODAS-2D average. A first trough (T_1) is observed at 26.8°E, flanking the Agulhas Plateau to the north. Average positions of additional meander troughs are 32.6°E (T_2) and 38.9°E (T_3), while crests are found at 29.7°E (C_1), 35.5°E (C_2), and 42.9°E (C_3).

The three meanders are also observed in RAFOS float trajectory segments (white dots and lines) or synoptic SSH snapshots (e.g. Fig. 3a and b), though the instantaneous positions can exhibit significant variability. In fact, meanders may temporarily disappear completely, particularly after shedding an eddy but in the long-term average, the meandering pattern prevails.

What amount of variability must be expected for the meander locations? Fig. 2, middle panel, shows the standard deviation of the MODAS-2D SSH field, with the highest variability, apart from the Agulhas Retroflection, observed along the mean path of the current (approximated by the 1.5 m average SSH anomaly). An estimate of the variability of the location is reflected in the area that falls between the 1.5 m SSH anomaly northerly extreme position (approximated by subtracting one standard deviation from the mean, dotted line in Fig. 2, bottom panel) and the southerly extreme position (approximated by adding one standard deviation to the mean, dashed line in Fig. 2, bottom panel). This graph indicates that the meandering path, though blurred, is nevertheless visible, particularly along its southern boundary. Along the average peak latitude of T_1 (37.5°S), for instance, one standard deviation includes the 25°–29°E longitude range for possible positions of T_1, while for T_2 the 31°–34°E range is observed along 38°S (Fig. 2, bottom). The location of trough T_3 (average peak latitude = 39°S) can merge in this analysis with T_2 and is limited to the east only, at 42.5°E. On the other hand, trough T_1 and T_2 are particularly well

Table 3

Locations (to the nearest tenth of a degree) of troughs and crests of the ARC. Positions were determined from 3-year mean MODAS-2D absolute sea-surface height estimates. Wavelengths are given to the nearest kilometer. The bottom rows present meander positions (to the nearest degree or half degree) given directly or deduced from images published in the literature by Lutjeharms and van Ballegooyen (1988) (L & VB) their Fig. 2, Quartly and Srokosz (1993) (Q & S), their Figs. 7 and A1, and Weeks et al. (1998) (W. et al.)

Feature	Trough 1	Crest 1	Trough 2	Crest 2	Trough 3	Crest 3	Period	Source
Longitude	26.8°E	29.7°E	32.6°E	35.5°E	38.9°E	42.9°E	Jan 97–Dec 99	MODAS 2D SSH
Wavelength		————500 km————		————543 km————				
Wavelength			————500 km————		————638 km————			
L & VB	27°E	30°E	33°E				Dec 84–Dec 85	METEOSAT IR
Q & S	26.5°E	29.5°E	32°E	34.5°E	38.5°E		Mar 85–Feb 88	AVHRR SST
W. et al.	26°E		32°E		38°E		Oct 91–Sep 94	AVHRR SST

defined by an area of exclusion located at 38.5°S and 30°E (Fig. 2, bottom, dotted circle). Crest C_1 falls between 27.5° and 32°E, while C_2 and C_3 are limited to the west only, at 34° and 39°E, respectively.

The location of the ARC meanders can be substantiated by a spatially resolved, time-integrated histogram of high velocity events within the MODAS-2D SSH field (Fig. 9). Using the gradient of the SSH field (i.e. the surface velocity field, see Boebel and Barron (2003) for details) avoids our previous subjective (but educated through the comparison with float and ADCP data) choice of the 1.5 m steric height anomaly as a proxy for the location of the current. The high-velocity data (speed $> 0.5\ \mathrm{m\ s^{-1}}$) are obviously outlining the path of the ARC and follow a zonal axis with a slight southward trend: 38°S at 25°E to 40°S at 45°E. Troughs and crests are found at the same position as in the averaged SSH field. Additionally, a higher frequency of speeds $> 0.5\ \mathrm{m\ s^{-1}}$ is observed along the connecting segments between troughs and crests in Fig. 9. Such behavior, i.e.

increased velocities within the connecting segments of meander extremes has been observed before in the Gulf Stream (Bower and Rossby, 1989) and the South Atlantic Current (Boebel et al., 1999, their Fig. 11), implicitly visible in the wider spacing of positions within the connecting segments).

What were the average meander locations during other periods? The location of T_1 is confirmed by the hydrographic study of Belkin and Gordon (1996). Additional studies based on remotely sensed sea-surface temperature measurements by Lutjeharms and van Ballegooyen (1988), Quartly and Srokosz (1993) and Weeks et al. (1998) provide strong support for our findings (Table 3), while spanning a period of 15 years. However, Weeks et al. (1998) cautiously note (p. 1623) "there is a hint" that this meandering pattern *could* be reversed during the summer. Such seasonal variability of meander positions cannot be corroborated by our results. Analysis similar to that shown in Fig. 2, but limited to austral summer (January–March) and winter (July–September)
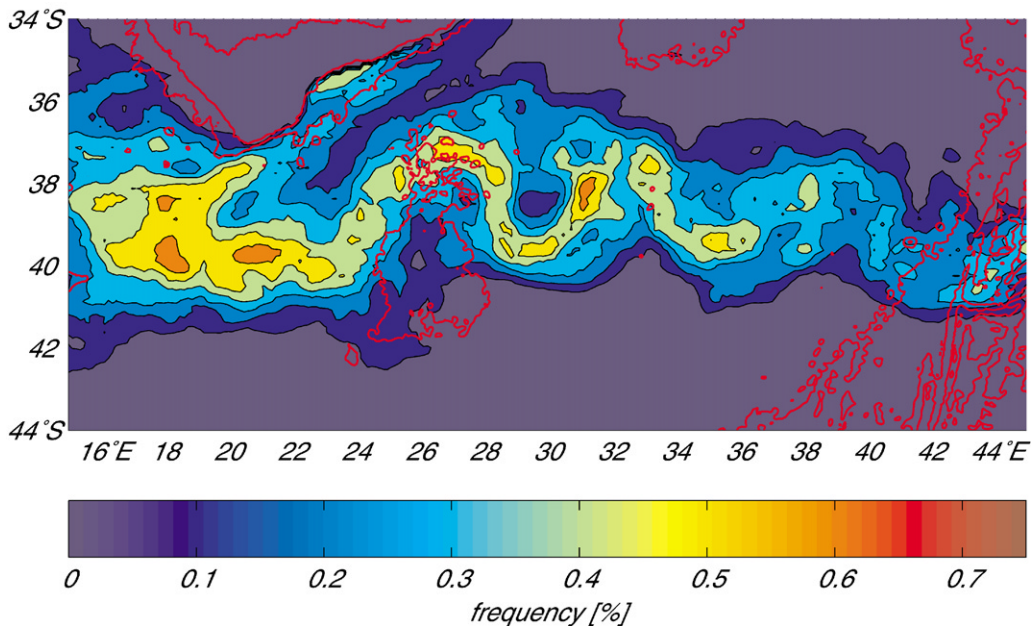

Fig. 9. Spatially resolved histogram of high velocity ($> 0.5\ \mathrm{m\ s^{-1}}$) data in the ARC region. Thin red lines indicate the coast as well as the 1000 and 3000 m isobaths.
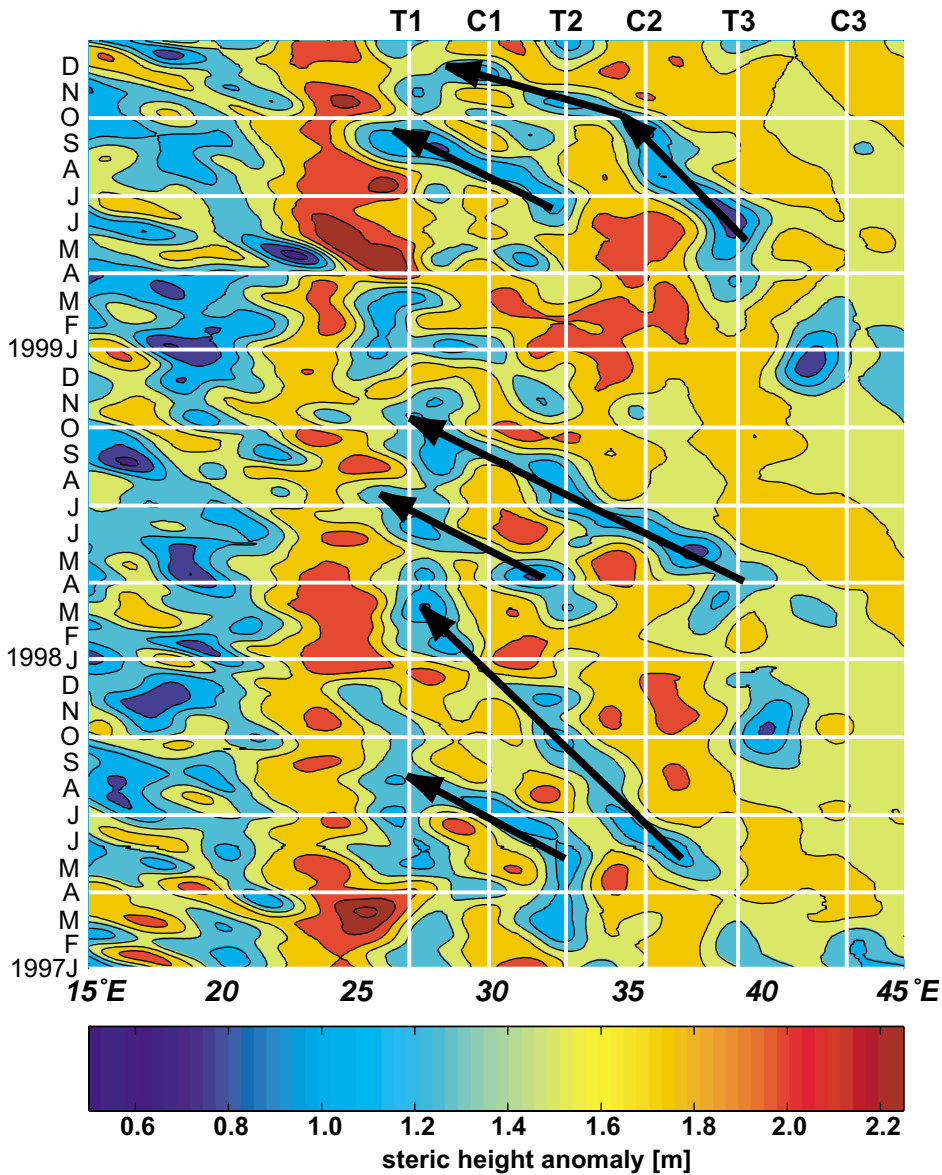
Fig. 10. Longitude-time (Hovmöller) diagram for MODAS sea surface steric height anomaly at 37.5°S. Steric height anomalies related to anticyclonic motion are red and anomalies related to cyclonic motion are blue. Black arrows indicate the migration of cyclonic eddies discussed in the text.

seasons, show stable meander positions for T_1, C_1 and T_2 (position vary by less than 1° longitude) and only small changes (order 1.5° longitude) for C_2 and T_3, while no change is observed for C_3. Such overall stability of meander positions also can be inferred by Quartly and Srokosz's (1993) seasonally resolved images of frequency of frontal occurrences (their Figs. 7 and A1). Rather than seasonal, the observed variability is dominated by changes on monthly time scales, which are clearly

observed when animating the MODAS-2D SSH field. Strong evidence exists that, on average, the first trough circumvents the Agulhas Plateau even at paleo-oceanographic time-scales. Uenzelmann-Neben (2002), based on sediment analysis, suggests that deep-reaching warm currents (i.e. the ARC or its predecessor) passed the Agulhas Plateau to the north since the Eocene, i.e. 35–57 Ma ago, suggesting a remarkable stability of this first meander.

Thus for nearly 15 years the ARC appears to have followed the same meandering pattern with three crests and troughs (not counting the retroflection itself) between the Agulhas Plateau and the Southwest-Indian Ridge. What causes the ARC to feature meanders and what stabilizes their position? A similar stability for example has not been observed in the corresponding Gulf Stream system where meanders propagate downstream. Obviously, the presence of the Agulhas Plateau is likely to act as stabilizing factor of the first meander trough position. However, whether this first meander of the ARC is exclusively generated and trapped by topographic steering is open to question. Modeling efforts without detailed bathymetry (Pichevin et al., 1999) produce a similar first trough east of the Retroflection, which at least hints towards an additional dynamical factor. Campos and Olson (1991) studied stationary Rossby waves in Western Boundary Current Extensions by means of an analytical model and numerical experiments. They point out that a *cum sole* tilt between the poleward axis and the WBC leads to a dominance of low or zero frequency, spatially damped waves in the extension regions. Such a preferential situation is met here, due to the southwestward orientation of the Agulhas Current, and a quasi-standing wave is indeed observed, i.e. the standing ARC meandering pattern discussed in this study.

While the stability of the long term mean path of the ARC is quite surprising, its temporal evolution raises even more questions. The analyses of daily MODAS-2DSSH data revealed an unexpected periodicity in the shedding and migration of cold-core eddies shed towards the north from ARC meander troughs. This is the subject of the next section.

4.2. Westward propagation of warm- and cold-core rings

During the 3 years of observation, a remarkable pattern of westward cyclonic eddy migration was observed from space (Fig. 10). During austral fall (around April/May) eddies were shed from both trough T_2 and T_3. Eddies shed from T_2 traveled west and merged with T_1 around September. Eddies shed from T_3 traveled synchronously to T_2, with which they merged only to detach again and continue to T_1. Trough T_1 was typically reached during the following austral spring.

A graphical representation of this cold-core ring migration along the northern edge of the ARC is provided by a Hovmöller (space-time) diagram (Fig. 10) of MODAS-2D SSH along 37.5°S latitude. This represents the typical latitude at which westward moving cyclones were observed in an animation of this data set.[2] It should be noted that the chosen latitude differs from that (i.e. 40°S) selected by others (Wang and Koblinsky, 1996; Matano et al., 1998), which are located along the southern boundary of the ARC regime. The Hovmöller diagram confirms the quasi-stationary meander positions (vertical stripes east of 25°E) and, additionally, the occasional westward propagation of cyclonic signals. The animation of this data set confirms that the phase propagating patterns are linked to the shedding and drift of eddies rather than the phase propagation of a meander.

A detailed description eddy by eddy is given in the Appendix, while Table 4 gives a summary of the events. Please note, that data in Table 4 are based on the (subjective) start and end points of the arrows in Fig. 10, while dates in the verbal description below refer to the SSH animation, i.e. the absorbance or shedding of a 1.5 m SSH contour loop. While this latter definition minimizes each period of ring existence, the interpretation of the Hovmöller diagram provides a better

---

[2] The animation can be obtained from the corresponding author or downloaded from Elsevier's DSR-II web portal at http://www.elsevier.com/locate/dsr2. Please follow the links to this issue's table of content where electronic annexes are linked. The movie (arc.avi) is provided as zip archive (arc.zip) of 27 Mbyte size with 912×504 pixels.

Table 4

Eddy propagation at 37.5°S. Data are taken from Fig. 10. Dates are rounded to half months, distances to the nearest degree longitude

Period	Duration (days)	From/To	Distance (km)	Average speed (cm s^{-1})
15 May '97–15 Aug '97	90	T_2–T_1	530	6.8
15 May '97–1 Mar '98	285	T_3–T_2–T_1	790	3.2
1 Apr '98–15 Jul '98	105	T_2–T_1	440	4.9
1 Apr '98–15 Oct '98	195	T_3–T_2–T_1	1060	6.3
15 Jun '99–15 Sep '99	90	T_2–T_1	530	6.8
15 Mar '99–15 Nov '99	180	T_3–T_2–T_1	970	6.6

view of the overall trends. Since no unique definition exists for when an eddy detaches or is absorbed, and since some eddies move to the north or south of 37.5°S, i.e. outside of the regime represented by Fig. 10, some minor inconsistencies between dates extracted from the two descriptions are not to be avoided.

Recapitulating the detailed descriptions of the Appendix and the information contained in Fig. 10, we observe that, even though significant variability is present between the events, eddies were shed each year simultaneously from T_3 and T_2, which, after traveling west, merged with the neighboring trough. Subsequently T_2 shed at least one eddy, which in part can be considered a descendant of the feature originally expelled from T_3. Eddies shed from T_3 typically (to the extent this word is justified with only three observations) had diameters > 200 km, while eddies shed from T_2 ranged between small (around 60 km) to mid-sized ($\approx$ 120 km).

The preferred migration path is reflected in the 3-year mean of sea-surface height standard deviations (Fig. 2, middle panel) by the increased variability linking T_3 to T_2 and T_2 to T_1, or alternatively, in the northern channel between T_2 and T_1 as outlined by the dotted 1.5 m of mean-sea-surface-height-minus-one-standard-deviation isoline. Contrastingly, neither of these observations can be made for the region south of the ARC, indicative of a lower number of warm, anticyclonic eddies in the subantarctic regime.

Anticyclonic eddies were occasionally shed from the currents crests, but had a short lifespan due to either re-absorption or dissipation (Lutjeharms, 1988). Of the five anticyclonic eddies observed,

which had a typical diameter of 100 km, three dissipated while two re-attached. A boundary for their maximum southerly extensions appears to be the 42°S parallel.[3]

One reviewer of this paper wondered whether the cyclones we claim to observe could be westward propagating Rossby waves (i.e. the ARC meanders themselves) rather than detached eddies. Firstly, the reviewer rightly argued that a clear distinction between eddies and growing, propagating meanders is difficult to make from a Hovmöller diagram only (Fig. 10). However, our supplemental animation of the daily SSH images shows that the signals observed in Fig. 10 are indeed related to propagating, detached eddies, as described in detail in the Appendix and Table 4. While these animations in our view resolve the ambiguousness of the Hovmöller diagram, the reviewer secondly continued to doubt the accurateness of MODAS-2D SSH as such.

The precision of the MODAS-2D SSH field is indeed of concern in this situation, since the addition of a false mean field, particular in regions of strong mean gradients, can be suspected of generating eddies when in reality only a growing meander exists. We therefore searched our data for events where the MODAS-2D SSH depiction of a detached eddy coincides with the acquisition of other data types. Fortunately one such eddy was transected during the 1997 Seward Johnson cruise.

---

[3] It should be noted that this is not in contradiction to the fact that the anticyclonic Agulhas Rings have larger diameters than the cyclones discussed herein. Agulhas Rings lie to the west of the Agulhas Retroflection, while the smaller anticyclones observed herein are found to the south of the ARC.

The ship borne ADCP data (Fig. 3a, eddy near $37°S$, $30°$) is here in clear support of the cyclonic pattern derived from the MODAS-SSH field, and the alternative concept of the eddy being part of troughs T_1 or T_2 appears unlikely. The concurrent XBT section (Fig. 4c) shows the shoaling of the $10°C$ isotherm by nearly 300 m from greater than 800 m between the ARC and the eddy to slightly deeper than 500 m in the core of the eddy. The animations reveal this eddy to be a residual product of the adsorption process by T_1 of the cyclone traveling from T_2 to T_1 in June/August 1997 (Table 4, first row).

Isopycnal floats responded to such cyclones on two occasions. In December 1998 and March 1999 floats drifting on the $\sigma_\theta = 26.8$ isopycnal clearly support the notion of closed streamlines within cyclonic features north of the ARC, with one float making three full revolutions in one of these eddies (see animation). Streamlines appear more open at greater depths, i.e. $\sigma_\theta = 27.2$ where floats can move more freely between the ARC and nearby eddies. Summarizing these multi-data observations in conjunction with the evidence that MODAS-2D SSH gives a highly realistic view of the mesoscale flow pattern of this region (Boebel and Barron, 2003), we consider the interpretation of the observed SSH anomalies as cyclonic eddies to be significantly more probable than the alternative description as westward propagating meanders.

Our observations of cyclonic eddies north of the ARC are not unprecedented. Cyclones have been observed in this region in independent SSH data (Gründlingh, 1995) and hydrographic sections (Lutjeharms and Valentine, 1984). The later study notes that the AF's "frontal structure is complicated by the recurrent eddy shedding in both meridional directions". In our study we clearly observe a more intense shedding of cyclonic cold-core eddies on the northern side than of anticyclonic warm-core eddies along the ARC's southern boundary. The westward propagation of cold-core eddies as suggested by data is corroborated by the study of Gründlingh (1995) as well. One cyclone was first observed near the nominal position of T_3 (at $37°S$, drifting from $40°E$ to $34°E$) while the other occurred near location where T_4 could be found ($44°E$), though this is east of our study region.

Preferred, concurrent shedding of meanders at two adjacent meander extremes could be explained by variations in the currents transport. Alternatively, as suggested by one reviewer, westward moving Rossby waves could be instrumental in the shedding process. However, with evidence for a seasonal intensification of the Agulhas Current or ARC (Pearce and Gründlingh, 1982; Ffield et al., 1997; Donohue and Firing, 2000) and the role of Rossby waves in this area (Matano et al., 1998, 1999) being sparse and controversial, and since our data do not provide sufficient additional insight, we refrain from speculating on these issues from an observational point of view. A recent comparative analysis of instabilities of the Parallel Ocean Program (POP) and Fine Resolution Antarctic Model (FRAM) (Wells et al., 2000) suggests that eddies are, in principal, shed from the northern edge of the ARC, mainly due to a barotropic instability mechanism. Westward moving eddies north of the ARC also were generated by the nonlinear reduced gravity model employed by Pichevin et al. (1999) to study the shedding of Agulhas Rings. While the latter authors discarded their finding as unrealistic, it fits in well with our observations.

5. Summary

This study reveals for the 1997–1999 period a spatially and temporally continuous Agulhas Return Current of 60–80 km width and volume flux within the core and above 1000 m of 44 ± 5 Sv. East (and upstream) of the Southwest-Indian Ridge the current flows between $38°$ and $40°S$ in a quasi-stationary meandering pattern. Peak surface velocities decreased from 2.1 m s^{-1} near the Agulhas Retroflection to 1.1 m s^{-1} around $32°E$. Cold-core eddies are shed nearly exclusively in austral fall from meander troughs T_2 and T_3, which then drift westward at an average speed of 5.4 cm s^{-1}. They are subsequently absorbed and reformed by the next meander upstream (T_2) and eventually absorbed by the permanent meander that wraps around the Agulhas Plateau (T_1).

Whether the synchronization and seasonal locking of the eddy shedding process is purely incidental, or if a seasonally coupled process could provide a dynamical explanation, remains to be addressed. Nevertheless, we showed substantial evidence by means of quasi-synoptic surveys, in situ float data and from altimetric measurements that the described flow patterns provide a realistic view of the ARC region[4] that can be employed beneficially to guide further oceanographic field studies.

---

[4] Daily MODAS-2D SSH images of this region are accessible by Internet from the Naval Research Laboratory at Stennis Space Center at http://www7300.nrlssc.navy.mil/altimetry/regions/reg_agl.html.

Appendix

To visualize the descriptions made below please consult the supplemental animation (see footnote #2 for access). Using QuickTime^{TM} will enable you to step through the movie frame by frame both forward and backward in time.

A.1. The 1997 eddies

On 20 March 1997 a small (diameter ≈ 60 km) eddy was shed from T_2. It quickly connected to T_1 a month later on April 21 (not listed in Table 4). Just prior to this eddy's absorption by T_1, another eddy was shed by T_2 on 19 April 1997, which immediately re-attached to T_2. It ultimately was shed on 23 June from T_2, and traveled west to connect with T_1 1 month later. By mid August the eddy and T_1 had merged completely (Table 4, row 1). Effectively all three shedding events materialized from a steep meander of T_2 that developed during February/March 1997.

On 6 May 1997 T_3 shed a large eddy of 140 km diameter (eddy diameters are estimated from the 1.5 m SSH anomaly contour). It traveled west and merged on 15 July 1997 with T_2 to form a steep meander. After considerable interaction with the surrounding eddy field, T_2 regurgitated the eddy, which had even grown in size to over 200 km diameter, connecting to T_1 on 25 January 1998 and merging with it in early February (Table 4, row 2).

A.2. The 1998 eddies

On 29 April 1998 a mid-sized eddy (diameter around 120 km) was shed from T_2. It merged with a similar sized eddy shed from T_1, only to connect to T_1 on 23 May 1998. Full merging with T_1 was achieved around 10 June 1998 (Table 4, row 3). Just prior to this, on 1 May 1998 a large eddy (diameter over 220 km) was shed from T_3, traveling westward to merge with T_2 during June. On 13 August 1998, this eddy was re-shed from T_2, loosing strength and size (new diameter around 100 km) during a short-lived attachment to T_1 on 27 August. Subsequently it briefly reattached to T_2 (*sic*!) in October 1998, to merge with another eddy

shed by T_1 in December 1998 and to finally connect to T_1 on 23 December 1998 (Table 4, row 4).

A.3. The 1999 eddies

Evolving from a relatively straight flow pattern during January/February 1999, the ARC troughs T_2 and T_3 steepened during March 1998, and a midsized (diameter 150 km) eddy was shed from T_2 on 12 April 1999. Within 2 weeks the eddy attached itself to T_1. However, during a rare event of shedding an anticyclonic eddy, part of T_1 becomes reincorporated into T_2, to result in another cyclone on 4 August 1999, which merges with an eddy shed concurrently by T_1 and had finally merged with T_1 by mid September (Table 4, row 5).

On 20 May trough T_3 shed a large (> 220 km diameter) eddy, which made contact with T_2 on 22 September 1999. T_2 regurgitated the eddy on 1 November 1999, which attached to T_1 on 13 November and was completely absorbed by T_1 in early December 1999 (Table 4, row 6).

References

Bang, N.D., 1970. Dynamic interpretations of a detailed surface temperature chart of the Agulhas Current retroflexion (sic) and fragmentation area. South African Geographic Journal 52, 67–76.

Belkin, I.M., Gordon, A.L., 1996. Southern Ocean fronts from the Greenwich meridian to Tasmania. Journal of Geophysical Research 101, 3675–3696.

Boebel, O., Barron, C.N., 2003. A comparison of in-situ float velocities with altimeter derived geostrophic velocities. Deep-Sea Research II, this issue (PII: S0967-0645(02)00381-8).

Boebel, O., Duncombe Rae, C., Garzoli, S., Lutjeharms, J., Richardson, P., Rossby, T., Schmid, C., Zenk, W., 1998. Float experiment studies interocean exchanges at the tip of Africa. EOS 79 (1), 6–8.

Boebel, O., Schmid, C., Zenk, W., 1999. Kinematic elements of Antarctic Intermediate Water in the western South Atlantic. Deep-Sea Research II 46, 355–392.

Boebel, O., Anderson-Fontana, S., Schmid, C., Ansorge, I., Lazarevich, P., Lutjeharms, J., Prater, M., Rossby, T., Zenk, W., 2000. KAPEX RAFOS Float Data Report 1997–1999; Part A: The Agulhas- and South Atlantic Current Components. Institut für Meereskunde an der Christian-Albrechts-Universität-Kiel, Berichte aus dem Institut für Meereskunde 318, Kiel, pp. 194.

Bower, A.S., Rossby, T.H., 1989. Evidence of cross-frontal exchange processes in the Gulf Stream based on isopycnal RAFOS float data. Journal of Physical Oceanography 19, 1177–1190.

Campos, E.J.D., Olson, D.B., 1991. Stationary Rossby Waves in Western Boundary Current Extensions. Journal of Physical Oceanography 21, 1202–1224.

Donohue, K.A., Firing, E., 2000. Comparison of three velocity sections of the Agulhas Current and Agulhas Undercurrent. Journal of Geophysical Research 105, 28585–28593.

Ffield, A., Toole, J.M., Wilson, W.D., 1997. Seasonal Circulation in the South Indian Ocean. Geophysical Research Letters 24, 2773–2776.

Fox, D.N., Teague, W.J., Barron, C.N., Carnes, M.R., Lee, C.M., 2002. The Modular Ocean Data Assimilation System (MODAS). Journal of Atmospheric and Oceanic Technology 19, 240–252.

Gründlingh, M.L., 1995. Tracking eddies in the southeast Atlantic and southwest Indian oceans with TOPEX/Poseidon. Journal of Geophysical Research 100, 24977–24986.

Hendry, R., 1988. A simple model of Gulf Steam thermal structure with application to the analysis of moored measurements in the presence of mooring motion. Journal of Atmospheric and Oceanic Technology 5, 328–339.

Jacobs, G.A., Barron, C.N., Rhodes, R.C., 2001. Mesoscale characteristics. Journal of Geophysical Research 106, 19581–19596.

Lutjeharms, J.R.E., 1988. Meridional heat transport across the sub-tropical convergence by a warm eddy. Nature 331, 251–254.

Lutjeharms, J.R.E., 1996. The exchange of water between the South Indian and South Atlantic Oceans. In: Wefer, G., Berger, W.H., Siedler, G., Webb, D. (Eds.), The South Atlantic: Present and Past Circulation. Springer, Berlin, Heidelberg, pp. 122–162.

Lutjeharms, J.R.E., Ansorge, I., 2001. The Agulhas Return Current. Journal of Marine Systems 30, 115–138.

Lutjeharms, J.R.E., Valentine, H.R., 1984. Southern Ocean thermal fronts south of Africa. Deep-Sea Research 31A, 1461–1475.

Lutjeharms, J.R.E., van Ballegooyen, R.C., 1984. Topographic control in the Agulhas Current system. Deep-Sea Research 31A, 1321–1337.

Lutjeharms, J.R.E., van Ballegooyen, R.C., 1988. The Retroflection of the Agulhas Current. Journal of Physical Oceanography 18, 1570–1583.

Matano, R., Simionato, C.G., Strub, P.T., 1999. Modelling the wind driven variability of the South Indian Current. Journal of Physical Oceanography 29, 217–230.

Matano, R.P., Simionato, C.G., de Ruijter, W.P., van Leeuwen, P.J., Strub, P.T., Chelton, D.B., Schlax, M.G., 1998. Seasonal variability in the Agulhas Retroflection region. Geophysical Research Letters 25, 4361–4364.

Olbers, D., Gouretski, V., Seiß, G., Schröter, J., 1992. Hydrographic Atlas of the Southern Ocean. Alfred Wegener Institute, Bremerhaven, 82pp.

Pearce, A.F., Gründlingh, M.L., 1982. Is there a seasonal variation in the Agulhas Current? Journal of Marine Research 40, 177–184.

Pichevin, T., Nof, D., Lutjeharms, J., 1999. Why are there Agulhas Rings? Journal of Physical Oceanography 29, 693–707.

Quartly, G.D., Srokosz, M.A., 1993. Seasonal variations in the region of the Agulhas Retroflection: studies with Geosat and FRAM. Journal of Physical Oceanography 23, 2107–2124.

Read, J.F., Pollard, R.T., 1993. Structure and transport of the Antarctic Circumpolar Current and Agulhas return current at 40 degree E. Journal of Geophysical Research 98, 12281–12295.

Rossby, T., Dorson, D., Fontaine, J., 1986. The RAFOS System. Journal of Atmospheric and Oceanic Technology 3, 672–679.

Schultz Tokos, K.L., Hinrichsen, H.H., Zenk, W., 1994. Merging and migration of two meddies. Journal of Physical Oceanography 24, 2129–2141.

Sparrow, M.D., Heywood, K.J., Brown, J., Stevens, D.P., 1996. Current structure of the South Indian Ocean. Journal of Geophysical Research 101, 6377–6391.

Stramma, L., 1992. The South Indian Ocean current. Journal of Physical Oceanography 22, 421–430.

Uenzelmann-Neben, G., 2002. Contourites on the Agulhas Plateau, SW Indian Ocean: indications for the evolutions of currents since Paleogene times. In: Stow, D., Pudsey, C., Thowe, J., Faugeres, J.C. (Eds.) Deep-water Contourites: Modern Drifts and Ancient Series, Seismic and Sedimentary Characteristics. Geological Society of London, pp. 271–288.

Wang, L., Koblinsky, C.J., 1996. Low frequency variability in the region of the Agulhas Retroflection. Journal of Geophysical Research 101, 3597–3614.

Webb, D.J., Kilworth, P.D., Coward, A.C., Thompson, S.R., 1991. The FRAM Atlas of the Southern Ocean, Natural Environmental Council, Swindon, p. 67.

Weeks, S.J., Shillington, F.A., Brundrit, G.B., 1998. Seasonal and spatial SST variability in the Agulhas retroflection and Agulhas return current. Deep-Sea Research I 45, 1611–1625.

Wells, N.C., Ivchenko, V.O., Best, S.E., 2000. Instabilities in the Agulhas Retroflection Current system: a comparative model study. Journal of Geophysical Research 105, 3233–3241.